

# Thermospheric weather as observed by ground-based FPIs and modeled by GITM

Brian J. Harding<sup>1</sup>, Aaron J. Ridley<sup>2</sup>, Jonathan J. Makela<sup>1</sup>

<sup>1</sup>Department of Electrical and Computer Engineering, University of Illinois at Urbana-Champaign, Urbana, IL, USA

<sup>2</sup>Climate and Space Sciences and Engineering, University of Michigan, Ann Arbor, MI, USA

## Key Points:

- A long-term data-model comparison of day-to-day thermospheric variability finds that GITM represents the weather poorly ( $-0.07 < \rho < 0.36$ )
- The average measured decorrelation time of 1.8 hours agrees with the modeled time of 1.9 hours
- The weather in GITM contains too little spatial structure, when compared with the measured ~1000 km decorrelation distance

This is the author manuscript accepted for publication and has undergone full peer review but has not been through the copyediting, typesetting, pagination and proofreading process, which

may lead to differences between this version and the Version of Record. Please cite this article as doi: [10.1029/2018JA026032](https://doi.org/10.1029/2018JA026032)

## Abstract

The first long-term comparison of day-to-day variability (i.e., weather) in the thermospheric winds between a first-principles model and data is presented. The definition of weather adopted here is the difference between daily observations and long-term averages at the same UT. A year-long run of the Global Ionosphere Thermosphere Model (GITM) is evaluated against a nighttime neutral wind dataset compiled from six Fabry-Perot interferometers (FPIs) at mid and low latitudes. First, the temporal persistence of quiet-time fluctuations above the background climate is evaluated, and the decorrelation time (the time lag at which the autocorrelation function drops to  $e^{-1}$ ) is found to be in good agreement between the data (1.8 hours) and the model (1.9 hours). Next, comparisons between sites are made to determine the decorrelation distance (the distance at which the cross-correlation drops to  $e^{-1}$ ). Larger FPI networks are needed to conclusively determine the decorrelation distance, but the current dataset suggests it is  $\sim 1000$  km. In the model the decorrelation distance is much larger, indicating that the model results contain too little spatial structure. The measured decorrelation time and distance are shorter than the scales expected if tidal forcing were responsible for the variability, suggesting that some other source is dominating the weather. Finally, the model-data correlation is poor ( $-0.07 < \rho < 0.36$ ), and the magnitude of the weather is underestimated in the model by 65%.

## 1 Introduction

A critical barrier to prediction of the thermosphere-ionosphere system is an understanding of the day-to-day variability of the thermosphere, which we refer to as thermospheric weather. Recent advances in the development of first-principles numerical ionosphere-thermosphere models and specification of the lower and upper boundary variability have enabled the possibility of capturing the weather, and the recent expansion of ground-based wind networks have enabled the validation of these models.

While models are still not perfectly representing the climate, progress has been made, as reported in long-term model-data comparisons [Meriwether *et al.*, 2013]. In contrast, comparisons of the weather are largely confined to case studies. For example, Sutton *et al.* [2007] compared eight days of cross-track wind estimates from the Challenging Minisatellite Payload (CHAMP) with the thermosphere-ionosphere-electrodynamics general circulation model (TIEGCM), finding a mean absolute difference of 64.1 m/s, slightly better than the comparison with the climatological horizontal wind model 2014 (HWM14). Wu *et al.* [2015] found that using the high-latitude variability prescribed by Super Dual Auroral Radar Network (SuperDARN) to drive the TIEGCM yielded better results than using the Heelis or Weimer models, in comparisons with ground-based wind measurements for a single storm period in Dec 2006. Wu *et al.* [2008] compared 10 days of TIEGCM runs from each of several years with ground-based wind observations in the polar cap, concluding that the TIEGCM overpredicted diurnal and semidiurnal oscillations. Emmert *et al.* [2001] developed an empirical model of daytime disturbance winds from Wind Imaging Interferometer (WINDII) data and compared it with the TIEGCM, finding important differences attributed mostly to high-latitude electric field variability. However, the Emmert *et al.* [2001] study averages data at a given local-time, latitude, season, solar flux, and Kp, focusing on the effect of geomagnetic disturbances on the background circulation. This differs from true weather due to the influence of tidal variability and waves propagating from high latitudes.

In this paper we take a long-term approach to evaluating thermospheric weather, comparing a year-long run of the Global Ionosphere Thermosphere Model (GITM) with observations. We focus particularly on the wind because not only is it a critical parameter in thermosphere-ionosphere coupling, but it also offers an extensive ground-based data source, namely networks of Fabry-Perot interferometers (FPIs). Previous studies have

64 compared GITM to space-based observations [Deng and Ridley, 2006; Mehta et al., 2017],  
65 but in this study we utilize ground-based data sources because a long time series from a  
66 single location allows for accurate removal of background climate. The disadvantage of  
67 ground-based wind data is that observations are restricted to nighttime. The only previ-  
68 ous study to compare GITM to ground-based thermospheric data sources is Liuzzo et al.  
69 [2015], which analyzed a case study of the 24 November 2012 substorm using different  
70 high-latitude drivers, comparing with the wind observed by Scanning Doppler Imagers at  
71 high latitudes. In this paper, we focus on mid and low latitudes. We also restrict our at-  
72 tention to quiet time weather ( $K_p \leq 3$ ) as it is understudied relative to storm time, and  
73 quiet conditions dominate the database.

74 GITM was run using inputs from 2013, and as such this paper discusses weather  
75 during a weak solar maximum. The solar cycle effect on climatological thermospheric  
76 winds at mid and low latitudes has been found to be small (0-50 m/s) [Fisher et al., 2015;  
77 Dandenault, 2018; Emmert et al., 2006]. The solar cycle effect on thermospheric weather  
78 is not known.

79 In the following sections, we describe the year-long GITM run, the instrumentation  
80 and observations, and our method of calculating the weather. Next, we investigate charac-  
81 teristics of the weather in the model and in the data, and we quantify how well the model  
82 is capturing the observed weather.

## 83 2 Model

84 GITM is a global model that describes the upper atmosphere of the Earth and its  
85 coupling to the ionosphere from 100 km altitude to approximately 500-600 km altitude,  
86 depending on solar activity [Ridley et al., 2006]. GITM solves the Navier-Stokes equations  
87 for the thermosphere, broken into vertical and horizontal directions. In the vertical direc-  
88 tion, a momentum and continuity equation is solved for each species. Coupling terms tie  
89 together the constituents in the lower thermosphere, and a bulk vertical wind is calculated  
90 given the mass-weighted average of the individual vertical winds. In the horizontal direc-  
91 tion, only a bulk momentum equation is solved for, with each species being advected with  
92 the bulk wind. For both the horizontal and vertical directions, ion drag, Coriolis, gradi-  
93 ent in pressure, and geometric terms are considered. In the horizontal direction, vertical  
94 shears are reduced with viscosity. Horizontal shears of the vertical winds are not consid-  
95 ered at this time because the scales are large in the horizontal direction and the vertical  
96 winds are often significantly smaller than the horizontal winds. In the vertical direction,  
97 gravity is considered.

98 GITM was run with  $4.0^\circ$  longitude by  $2.5^\circ$  latitude by roughly 0.3 scale height res-  
99 olution. The altitude spacing in GITM was based on scale heights determined from MSIS  
100 temperature and mean major mass results for the dayside equator at the start time of each  
101 simulation. The time step in GITM was roughly two to three seconds and was dynami-  
102 cally set based on the speed of sound, ion and neutral wind speeds and the size of each  
103 cell in all three dimensions. In the majority of cases, the timestep was limited due to the  
104 smallest altitude spacing and the speed of sound.

105 The GITM runs were driven by NRLMSISE-00 [Picone et al., 2002] and HWM14  
106 [Drob et al., 2015] at the lower boundary, and Weimer [2005] electric potential patterns  
107 and Newell et al. [2014] auroral precipitation patterns at the upper boundary. Both the po-  
108 tential and the aurora were driven by interplanetary magnetic field and solar wind data.  
109 Daily averaged solar irradiance specifications from FISM were used. Table 1 specifies  
110 the inputs that were used for the simulation. GITM is freely available for download on  
111 GitHub.

112 Because of the time-step in GITM and some of the complexities in the chemistry  
113 and advection schemes, GITM typically runs roughly ten times faster than real time at this

125

**Table 1.** GITM parameters for the simulations presented in this study

Parameter	Value
Eddy Diffusion Coefficient	300
Eddy Pressure Lower	0.005
Eddy Pressure Upper	0.0005
Photoelectron Heating Efficiency	0.00
Neutral Heating Efficiency	0.05
Thermal Conduction (Molecular)	5.6e-4
Thermal Conduction (Atomic)	7.6e-4
Thermal Conduction Power	0.72
AUSMSolver	True
CFL	0.80
Limiter	MC, 2.0
Dynamo High Lat. Boundary	45.0
Improved Ion Advection	True
Nighttime Ion B.C.s	True
Minimum TEC for Ion B.C.s	2.0
UseTestViscosity	True
TestViscosityFactor	1.0

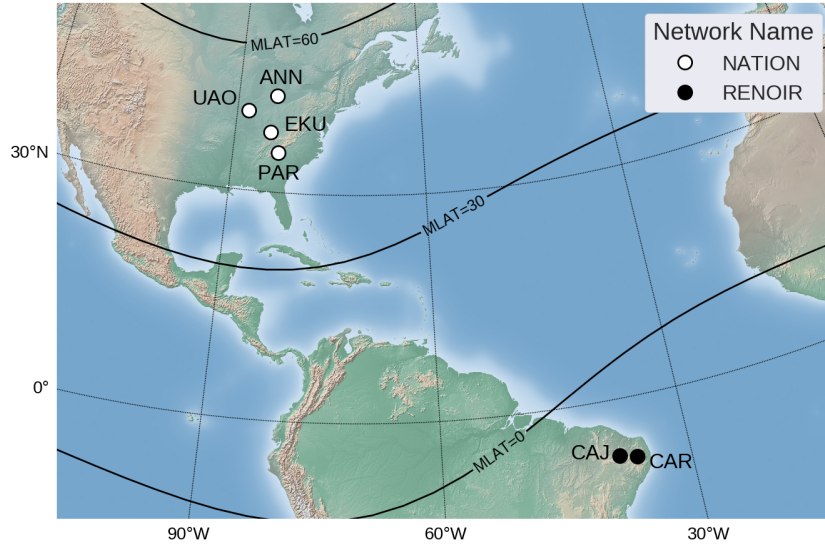
114 resolution. This means that in order to run a full year continuously, it would take roughly  
 115 37 days. To mitigate this, each month was run individually. This means that GITM was  
 116 started on the first day of each month, and was run for the complete month. The run was  
 117 allowed to continue into the next month for about three days, and the first three days of  
 118 the simulation were swapped for the last three days of the previous month's run. For ex-  
 119 ample, for March, the first three days of March were deleted for the March run and first  
 120 three days of March were used from the last days of the February run.

121 A second large run was performed, spanning most of 2013, with higher resolution  
 122 in the latitudinal direction ( $1.0^\circ$  instead of  $2.5^\circ$ ). While there were differences in the re-  
 123 sults, the main conclusions of the study reported here were not altered. We use the lower  
 124 resolution model here because it covers all of 2013.

### 126 3 Instrumentation and Observations

127 This study uses data from six ground-based (FPIs) at mid and low latitudes in the  
 128 American sector, as shown in Figure 1. The FPIs make narrow-field-of-view measure-  
 129 ments of naturally occurring 630.0 nm airglow, which is emitted in a layer around 250  
 130 km altitude. Estimates of the Doppler shift and width of this emission are a measure of  
 131 the line-of-sight (LoS) thermospheric wind and temperature. The instrument design is  
 132 described in detail by *Meriwether et al.* [2011]. The six FPIs are organized into two net-  
 133 works: the North American Thermosphere-Ionosphere Observing Network (NATION),  
 134 described by *Makela et al.* [2014], and the Remote Equatorial Night-time Observatory of

135 Ionospheric Regions (RENOIR), described by *Makela et al.* [2013]. Although the database  
 136 includes many years of data, in this paper we use 2013 to match GITM.



137 **Figure 1.** Locations, site codes, and network names for the six FPI sites used in this study. Magnetic  
 138 latitude (MLAT) is also shown.

139 These FPIs operate by cycling through a variety of look directions, including oc-  
 140 casional observations of a frequency-stabilized laser for calibration. A variety of operat-  
 141 ing modes were used in 2013, including cardinal mode (which cycles through north, east,  
 142 south, and west, at a 45-deg zenith angle, followed by zenith) and common-volume mode  
 143 (which optimizes look directions to observe the same location from different sites); see  
 144 *Makela et al.* [2013] for more details. In this work, each instrument is analyzed for winds  
 145 independently. The dataset also includes an operational mode with a constant exposure  
 146 time (usually set to 180, 210, or 300 seconds) as well as a mode that adjusts the exposure  
 147 time to maintain a constant measurement uncertainty.

### 148 3.1 Analysis

149 Each observation's raw data are analyzed using the algorithm described by *Harding*  
 150 *et al.* [2014] to obtain LoS wind estimates, which are ascribed to an altitude of 250 km.  
 151 To convert the various LoS wind observations from a single instrument into an estimate  
 152 of the zonal and meridional wind, the LoS data are first collected in half hour bins. Half  
 153 hour bins were chosen to match the GITM samples. The zonal and meridional directions  
 154 refer to a geographic coordinate system. The unknown zonal wind,  $u$ , meridional wind,  $v$ ,  
 155 and Doppler reference,  $\Delta d$ , in each bin are fit in the least-squares sense (accounting for  
 156 measurement uncertainties) to the following observation model:

$$d_i = u \sin \theta_i \sin \phi_i + v \cos \theta_i \sin \phi_i + \Delta d \quad (1)$$

157 where  $d_i$  is the  $i^{\text{th}}$  LoS wind in the bin,  $\theta_i$  is the azimuth angle of that measurement, and  
 158  $\phi_i$  is the zenith angle. On average, 8 LoS observations contribute to each estimate of  $u$ ,  $v$ ,  
 159 and  $\Delta d$ , though it ranges from 3 to 27. The assumption is that the vertical wind is zero.  
 160 This differs from the procedure used in previous studies, which allowed for the estimation  
 161 of time-dependent vertical winds, but which also required an assumption that the aver-  
 162 age vertical wind over a night is zero [e.g., *Makela et al.*, 2013]. In this study, we assume

163 that the instantaneous vertical wind is zero, as this allows  $\Delta d$  to vary. Ideally, the time-  
164 dependence of  $\Delta d$  is accounted for by frequent laser calibration observations, but allowing  
165  $\Delta d$  to vary better handles non-ideal cases such as laser drift, instrument fluctuations that  
166 are more rapid than the calibration cadence, and most importantly, contamination by emis-  
167 sion lines such as OH which are not addressed by the quality control algorithm (described  
168 below). The binned least-squares procedure is general enough to handle data from both  
169 cardinal and common-volume modes of operation.

170 We multiply all horizontal winds by 1.10 to correct for the scattering of airglow in  
171 the troposphere, as recommended by *Harding et al.* [2017]. This does not affect any re-  
172 ported correlations, but it reduces the normalized standard deviations in Figure 5. This  
173 simple correction is appropriate for cases with no horizontal airglow gradients. In the  
174 dataset used here, the variation of airglow brightness measured in different directions is on  
175 average 28%, so the correction should likely be larger and depend on direction. However,  
176 it cannot be evaluated without colocated all-sky imagers at each site and prohibitively ex-  
177 pensive computation.

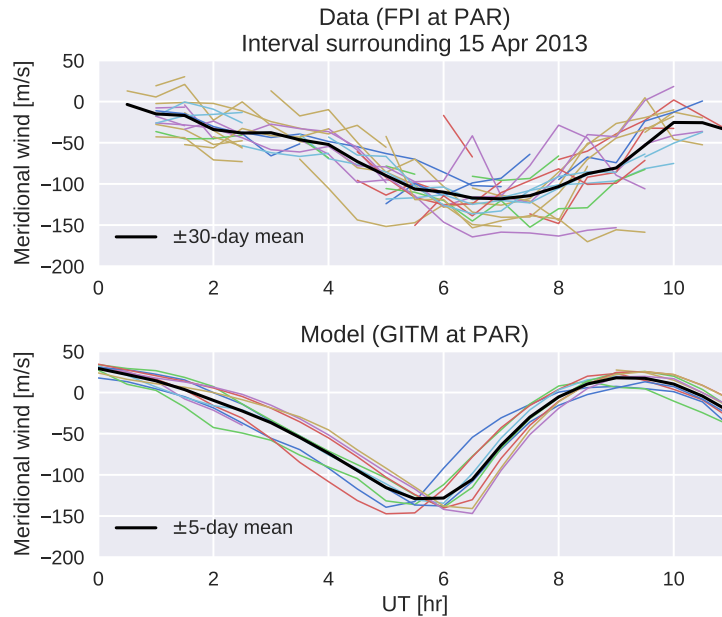
### 178 3.2 Quality Control

179 The quality control algorithm first removes all LoS measurements with temperatures  
180 less than 150 K or uncertainties greater than 100 m/s or 100 K, as these indicate poor raw  
181 data quality or poor fringe fitting. Samples for which the continuum background spectrum  
182 contribution is more than 0.4 counts/s are considered to be contaminated by moonlight  
183 and are removed. It is well known that when the 630.0 nm emission is dim, the nearby  
184 OH emissions at 629.8 nm and 630.7 nm have a contaminating effect upon the winds  
185 [*Hernandez, 1974; Ronksley, 2016*], and the effect depends upon the characteristics of the  
186 instrument's interference filter. We remove samples for which the measured brightness is  
187 below a predetermined instrument-dependent threshold, chosen by binning historical zenith  
188 observations by brightness, and choosing the brightness for which the measured wind de-  
189 viates from zero by more than 20 m/s.

190 A second quality control step is implemented after the binning and conversion from  
191 LoS to horizontal winds. Bins for which the least-squares fit is deemed untrustworthy  
192 (matrix condition number greater than 10, root-mean-square (RMS) residual greater than  
193 50 m/s, or propagated uncertainty greater than 50 m/s) are removed. To focus on quiet  
194 times, bins for which the maximum value of  $K_p$  in the previous 24 hours is greater than  
195 3 are eliminated. Bins which contain any samples deemed cloudy are removed. Cloud  
196 detection is implemented using a colocated Boltwood cloud sensor, which measures the  
197 ambient temperature and the infrared sky temperature. When the infrared temperature mi-  
198 nus the ambient temperature is greater than a threshold, cloudy conditions are indicated.  
199 The best choice for this threshold is not obvious, and some analyses (not shown) have sug-  
200 gested that it may depend on site and season. In the absence of any justification for which  
201 functions to use, in this work we use a scalar threshold of  $-22^\circ\text{C}$ . Although the manu-  
202 facturer recommends a threshold of  $-25^\circ\text{C}$ , we find that this results in nearly all summer  
203 days at UAO and PAR to be considered cloudy. Although many of the quality control pa-  
204 rameters listed above are somewhat arbitrarily chosen, the same qualitative conclusions are  
205 reached when other reasonable parameters are used. After quality control, 490–790 hours  
206 of data are available per instrument, which represents about 25% of the raw data set.

## 207 4 Results and Discussion

212 We take the modeled and observed horizontal winds for 2013 and first calculate the  
213 weather. For the model, the weather at a particular time is defined by subtracting the av-  
214 erage wind at the same time of day in  $\pm 5$ -day window. Bins which do not contain at least  
215 7 samples for defining the climate are removed. For the data, a  $\pm 30$ -day window is used.  
216 Although ideally the same window length would be used, a shorter window than  $\pm 30$  days



208 **Figure 2.** Meridional wind during an interval surrounding 15 Apr 2013. Thin, colored lines denote the  
 209 wind from individual nights in the data (top) and model (bottom). An interval of 60 days is shown for the  
 210 data, while 10 days are shown for the model. The thick black line is the computed background climate. Statis-  
 211 tical errors in the data range from 4 to 40 m/s, averaging 12 m/s.

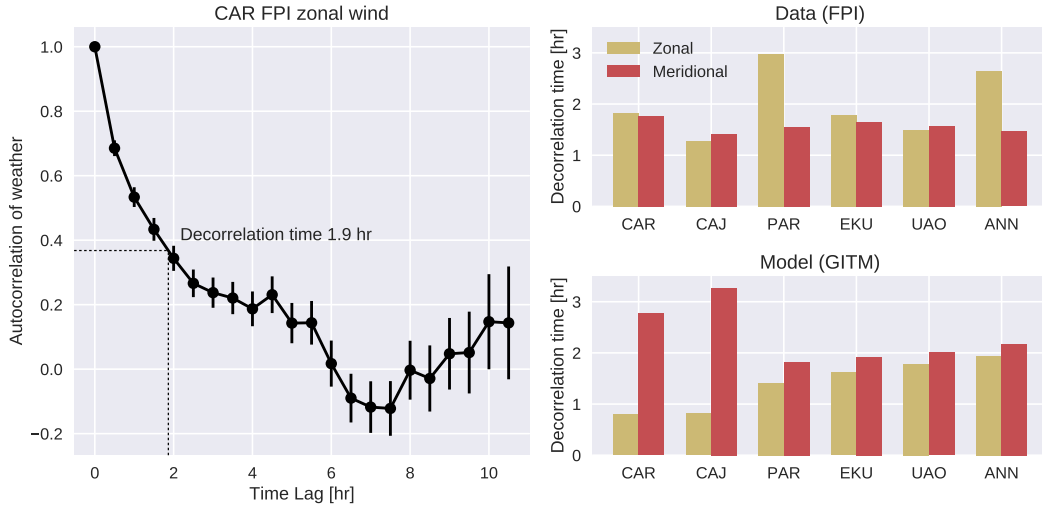
217 is not supported by the data density, and if a longer window is used for the model, the re-  
 218 sulting weather is dominated by a monthly artifact arising from the model restart, not the  
 219 true day-to-day variability. The underlying cause of the artifact is unknown but under in-  
 220 vestigation. Different quantitative results are obtained for different definitions of climate  
 221 (e.g., a  $\pm 10$ - instead of  $\pm 5$ -day window), but the qualitative conclusions are unchanged.

222 Figure 2 shows observed and modeled meridional winds from an interval surround-  
 223 ing 15 Apr 2013. Each thin colored line contains data from one night, and the thick black  
 224 line is the calculated background climate. The weather is defined as the difference. We  
 225 emphasize that features such as unvarying tidal structures (e.g., diurnal, semidiurnal, etc.)  
 226 would not be included in the following analysis, since they would be subtracted as part  
 227 of the climate. It is only the day-to-day variations in these tides that would be considered  
 228 weather in this study. In the following sections, we answer the questions: when there is a  
 229 disturbance from the background climate, how long does it last, how widespread is it, and  
 230 how well does the model capture the disturbance?

#### 231 4.1 Decorrelation Time

235 To quantify the temporal persistence of the weather, we calculate its autocorrelation  
 236 function. An example for the CAR zonal wind is shown in the left panel of Figure 3. The  
 237 correlation decreases with increasing time lag, and the time lag at which the correlation  
 238 drops to  $e^{-1}$  is 1.9 hours. We refer to this as the decorrelation time. Past this time delay,  
 239 the fluctuations about the background climate can be considered uncorrelated.

240 The right panel of Figure 3 displays the decorrelation times for the zonal and meridional  
 241 winds at all sites, in both the data and the model. On average, the model and the  
 242 data agree remarkably well, with decorrelation times of 1.9 and 1.8 hours, respectively. In  
 243 the model, at midlatitudes (PAR, ECU, UAO, and ANN), zonal and meridional decorre-



232 **Figure 3.** (Left) The measured time-lagged autocorrelation function for the CAR zonal wind weather, with the  
 233 computed decorrelation time. (Right) The decorrelation time at all sites in both the zonal and meridional  
 234 wind for the data (top) and model (bottom).

244 lation times are nearly identical, yet at low latitudes (CAR and CAJ), the zonal decorre-  
 245 lation time is much shorter. No evidence for this is seen in the data, for which the zonal  
 246 and meridional decorrelation times are similar at all sites, except for the PAR and ANN  
 247 zonal wind, which are larger. ANN and PAR are the northernmost and southernmost sites  
 248 in the midlatitude network, so there does not appear to be any physical reason why their  
 249 decorrelation times are longest.

## 250 4.2 Decorrelation Distance

251 To quantify the spatial scale spanned by structures in the weather, we compute the  
 252 cross-correlation between sites. In comparing the model results with the data, we must  
 253 take care to account for noise in the data. For example, if two sites observe exactly the  
 254 same weather but encounter different noise, the correlation is less than one. Assuming  
 255 the propagated uncertainties are correctly estimated, this effect can be corrected by using  
 256 a modified cross-correlation. The standard Pearson correlation coefficient between two  
 257 measurements  $y_1$  and  $y_2$  can be written as

$$\rho = \frac{\langle y_1 y_2 \rangle}{\sqrt{\langle y_1^2 \rangle} \sqrt{\langle y_2^2 \rangle}} \quad (2)$$

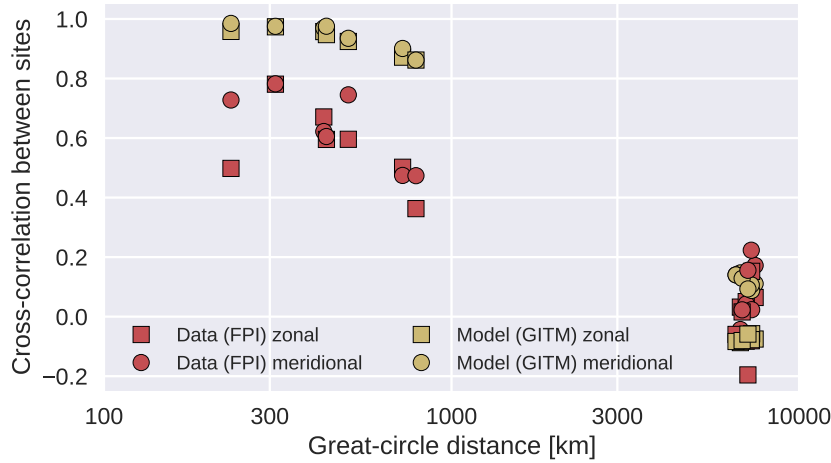
258 where  $\langle \cdot \rangle$  denotes ensemble or temporal average. In the case where the measurement is  
 259 a combination of signal and noise ( $y = s + n$ ), the noise is uncorrelated with the signal,  
 260 the noise is uncorrelated between sites, and the noise power  $\langle n^2 \rangle$  is known, the modified  
 261 correlation coefficient can be calculated as

$$\rho' = \frac{\langle y_1 y_2 \rangle}{\sqrt{\langle y_1^2 \rangle - \langle n_1^2 \rangle} \sqrt{\langle y_2^2 \rangle - \langle n_2^2 \rangle}}. \quad (3)$$

262 For this dataset,  $\rho'$  is larger than  $\rho$  by about 10–20%.

265 Figure 4 shows the modified cross-correlations for all pairs of sites, as a function  
 266 of baseline (i.e., great-circle distance between the sites). In general, the trend is smaller





263 **Figure 4.** Cross-correlations for all pairs of sites, for both the zonal and meridional wind in the data and the  
 264 model.

267 correlations for longer baselines, with correlations over the long distances between NA-  
 268 TION and RENOIR near zero. The modeled weather has much higher correlation than the  
 269 data, suggesting that the model is smoothing over spatial structure that is observed in real  
 270 weather.

271 Without longer baselines than those available within RENOIR or within NATION,  
 272 it is impossible to conclusively evaluate the decorrelation distance (the baseline at which  
 273 the cross-correlation drops to  $e^{-1}$ ). Nevertheless, upon extrapolation, the data suggest a  
 274 decorrelation distance of roughly 1000 km.

275 The closest baseline is CAJ-CAR at 232 km. While the CAJ-CAR meridional correla-  
 276 tion (0.73) fits the general trend well, the low zonal correlation (0.50) appears to be an  
 277 outlier. Despite much effort, no explanation is apparent, but we suspect that this is caused  
 278 by a cloud detection problem. This would explain why the zonal wind is affected more  
 279 than the meridional wind. The zonal wind is generally larger, and the presence of clouds  
 280 brings the measured wind toward zero. Cloud cover at CAJ but not CAR would cause  
 281 large differences in the zonal wind. However, the correlation is low for a variety of cloud  
 282 detection thresholds, as well as seasonally dependent thresholds, so the cause of this low  
 283 correlation remains unknown.

284 If the weather were dominated by day-to-day tidal variability, the decorrelation dis-  
 285 tance would be expected to take on global scales larger than 1000 km. Combined with the  
 286 relatively short decorrelation times reported above, this suggests that the weather in the  
 287 thermosphere is dominated by some other source than tidal variability, possibly large-scale  
 288 gravity waves generated by high-latitude heating (often called traveling atmospheric distur-  
 289 bances).

290 It should be noted that the estimates of  $\langle n_1^2 \rangle$  and  $\langle n_2^2 \rangle$  used in (3) contain statisti-  
 291 cal noise only. Systematic errors can arise as a consequence of OH contamination, atmo-  
 292 spheric scattering, rapid ambient temperature changes, and uncertainty in the layer alti-  
 293 tude, among other sources. However, the quantification of these errors is too uncertain to  
 294 include in this analysis. If they were included, they would increase the correlations shown  
 295 in Figure 4, but it is unlikely they would change the conclusion that the decorrelation dis-  
 296 tance is less than tidal scales.

297 A caveat of this analysis is that the wind estimate uses oblique measurements, which  
298 sample the thermosphere at locations horizontally removed from the site location. For ex-  
299 ample, in cardinal mode, the pierce points of the north-, east-, south-, and west-observing  
300 directions are 250 km away. Because of this, the true cross-correlations for baselines less  
301 than about 500 km are likely lower than reported here.

302 One might expect that given the relatively short decorrelation times and distances,  
303 weather may arrive at different sites at different times. To address this, we performed  
304 a time-lag analysis. The time-lagged cross-correlation functions are broad (1–3 hours)  
305 and peaked at or near zero, so adding a time lag does not significantly change the results  
306 shown in Figure 4.

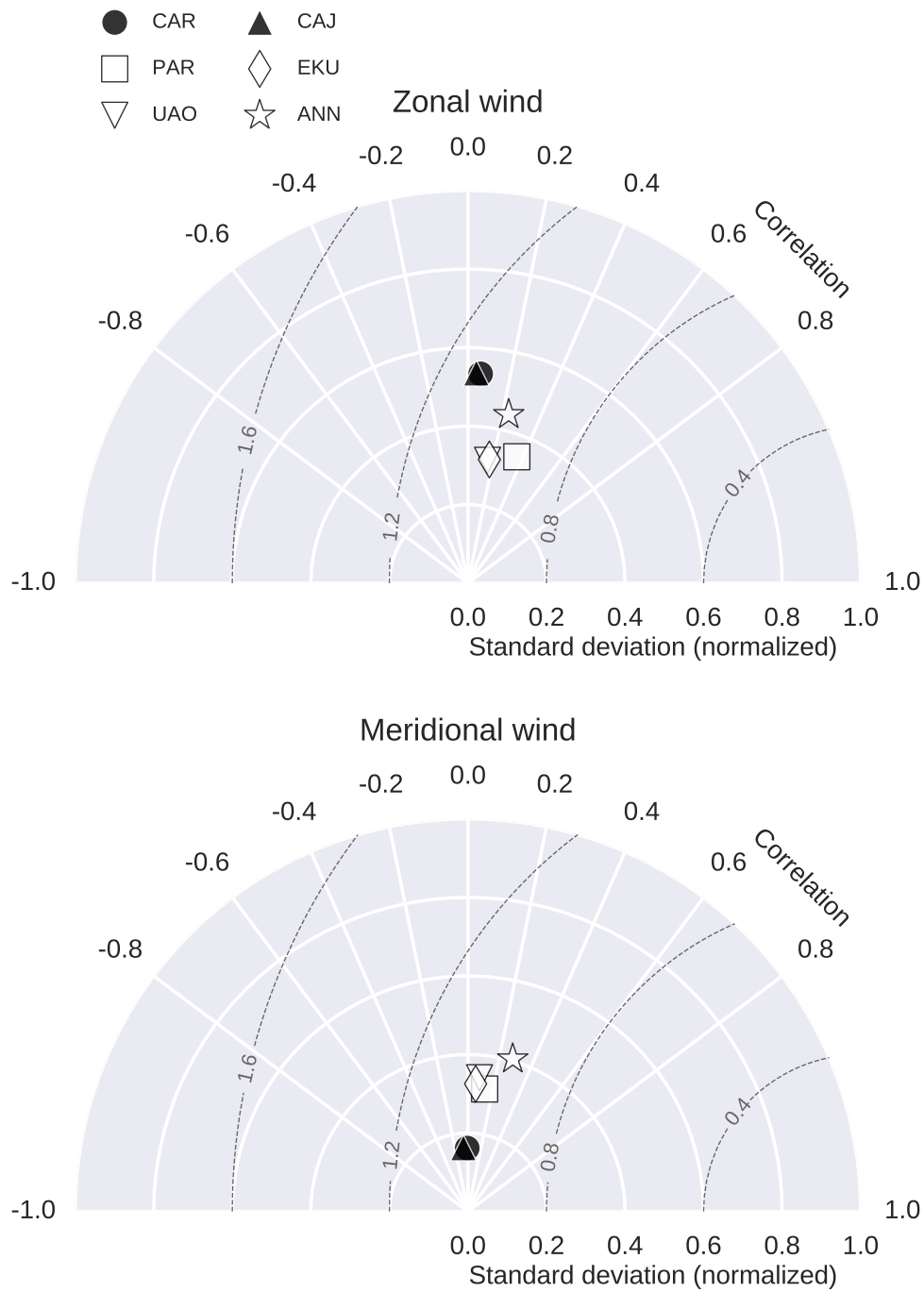
### 307 4.3 Model-Data Correlation

308 The previous two subsections compared the statistics of the modeled weather with  
309 the statistics of the observed weather. This section quantifies how well the weather com-  
310 pares on a day-to-day basis. To evaluate GITM's performance in capturing the weather we  
311 use Taylor diagrams [Taylor, 2001], which have previously been applied to space physics  
312 by Elvidge *et al.* [2014]. Taylor diagrams combine two commonly used metrics for model  
313 performance, correlation and RMS error, using the fact that their relationship resembles  
314 the law of cosines.

319 The Taylor diagrams for GITM's zonal and meridional weather are shown in Fig-  
320 ure 5. Each is a polar plot where the angle is arccosine of the model-data correlation,  
321 which is calculated including a modification like in (3) to account for noise in the data.  
322 The radius is the standard deviation of the modeled weather, divided by the standard devi-  
323 ation of the observed weather. Again, a correction is included to remove the noise power.  
324 The dashed contours are RMS error, normalized to the standard deviation of the observed  
325 weather. A perfect model with zero error is located at the lower right corner, with a corre-  
326 lation of 1.0 and a normalized standard deviation of 1.0.

327 Immediately evident in Figure 5 is the large RMS error of  $\sim 1.0$ , indicating that the  
328 model error is of the same magnitude as the observed weather. The model error is un-  
329 derstood in terms of two sources. First, the modeled weather is too small, with a normal-  
330 ized standard deviation of 0.35 on average, indicating that the magnitude of the weather  
331 is underestimated by 65% in the model. The low latitude meridional wind fluctuations are  
332 particularly underestimated in the model (0.16). Second, the correlations are low, rang-  
333 ing from -0.07 to 0.36. The uncertainty in the reported correlations is  $\sim 0.03$ . In general,  
334 for both the zonal and meridional wind, the low latitude correlations (insignificantly dif-  
335 ferent from zero) are less than the mid latitude correlations (0.19 on average). The mid  
336 latitude correlations are small yet statistically significant, indicating that while GITM's  
337 performance in capturing the weather is quite poor, it is at least representing some of the  
338 relevant physics at mid latitudes. This is perhaps surprising given the relative simplicity of  
339 the lower-boundary and high-latitude forcing in the model. Especially at low latitudes, the  
340 performance may be improved by including data-driven lower boundary tidal variability,  
341 but the short decorrelation distances and times in the data suggest this would not address  
342 the dominant type of weather.

343 Unlike the previous results, which were based on correlations, the standard devi-  
344 ations are sensitive to the assumed emission altitude of 250 km. A sensitivity test was  
345 performed in which the winds were extracted from the model at two other altitudes, 210  
346 km and 290 km. The normalized standard deviations were 25–50% lower at 210 km com-  
347 pared to 290 km, indicating that the magnitude of the weather is larger at higher altitudes.  
348 However, using a different altitude than 250 km does not change the conclusion that the  
349 magnitude of the weather is underestimated in the model.



315 **Figure 5.** Taylor diagrams evaluating the model performance in the zonal (top) and meridional (bottom)  
 316 weather. The angular coordinate represents model-data correlation and the radial coordinate represents mod-  
 317 eled weather standard deviation divided by observed weather standard deviation. The RMS error can be  
 318 calculated from these two values and is shown in dashed contours.

## 5 Conclusion

We have presented the first long-term comparison of thermospheric weather between a first-principles numerical model and data. Using nighttime thermospheric wind data from 2013 at six FPI sites at mid and low latitudes, we have characterized fluctuations about the climate during quiet times, focusing on three questions: how long do fluctuations last, how widespread are they, and how well does the model reproduce the observed weather? The data indicate an average decorrelation time of 1.8 hours and suggest a decorrelation distance of about 1000 km. The weather in the model (GITM) has a remarkably similar decorrelation time of 1.9 hours, but nearby sites are much more correlated than in the data, suggesting that the modeled weather is too smooth spatially but has the correct temporal persistence. The short decorrelation time and distance in the data suggest that the dominant mode of variability is not tidal.

The model's ability to capture day-to-day variations in the weather is poor. It underestimates the magnitude of the weather by 65%. Averaged between the zonal and meridional wind, model-data correlations are near zero at low latitudes and 0.19 at mid latitudes. Clearly, much work remains to model thermospheric weather, and our work suggests that focusing on high-latitude drivers is likely to be more successful than improving lower boundary tidal forcing.

These results could be useful for assimilative models, at least for the regions studied here (mid and low latitudes in the American sector). Most assimilative models have a notion of model covariance, which characterizes the temporal and spatial scales over which incoming measurements should inform the next estimate. The reported decorrelation time and distance could help tune model covariance, as there is a clear analogy between our definition of weather and the innovation sequence used in Kalman filters.

The site-to-site cross-correlations in Figure 4 reveal a significant gap in our understanding of the weather on scale sizes between 790 km (the longest baseline in NATION) and ~7000 km (the distance between NATION and RENOIR). They also suggest that the NATION FPIs are not optimally distributed. For example, the EKV-PAR correlation (baseline 311 km) is 0.78, so most of the information would have been captured by just one site. If the goal is to maximize the observability of fluctuations in the thermospheric wind, future deployments should target longer baselines.

## Acknowledgments

The FPI data in this work are available on the Madrigal database or can be made available by request. The Kp data used were obtained from the National Oceanic and Atmospheric Administration's National Centers for Environmental Information. Work at the University of Illinois was supported by NSF grant AGS 14-52291. The authors recognize the NATION and RENOIR teams for support hosting and maintaining the instruments. At the University of Michigan, the research was supported through the NSF grant ATM-1452097, and AFOSR under DDDAS (Dynamic Data-Driven Applications Systems, <http://www.1dddas.org/>) grant FA9550-16-1-0071. The simulations were conducted on NASA Pleiades.

## References

- Dandenault, P. B. (2018), MENTAT: A New Wind Model for Earth's Thermosphere, *Journal of Geophysical Research: Space Physics*, 123, doi:10.1029/2018JA025551.
- Deng, Y., and A. J. Ridley (2006), Dependence of neutral winds on convection E-field, solar EUV, and auroral particle precipitation at high latitudes, *Journal of Geophysical Research: Space Physics*, 111(9), 1–18, doi:10.1029/2005JA011368.
- Drob, D. P., J. T. Emmert, J. W. Meriwether, J. J. Makela, E. Doornbos, M. G. Conde, G. Hernandez, J. Noto, K. A. Zawdie, S. E. McDonald, J. D. Huba, and J. H. Klenz-

- 399 ing (2015), An update to the Horizontal Wind Model (HWM): The quiet time thermo-  
400 sphere, *Earth and Space Science*, 2(7), 301–319, doi:10.1002/2014EA000089.
- 401 Elvidge, S., M. J. Angling, and B. Nava (2014), On the use of modified Taylor diagrams  
402 to compare ionospheric assimilation models, *Radio Science*, 49(9), 737–745, doi:  
403 10.1002/2014RS005435.
- 404 Emmert, J. T., B. G. Fejer, C. G. Fesen, G. G. Shepherd, and B. H. Solheim (2001), Cli-  
405 matology of middle- and low-latitude daytime F region disturbance neutral winds mea-  
406 sured by Wind Imaging Interferometer (WINDII), *J. Geophys. Res.*, 106(A11), 24,701,  
407 doi:10.1029/2000JA000372.
- 408 Emmert, J. T., M. L. Faivre, G. Hernandez, M. J. Jarvis, J. W. Meriwether, R. J. Niciejew-  
409 ski, D. P. Sipler, and C. A. Tepley (2006), Climatologies of nighttime upper ther-  
410 mospheric winds measured by ground-based Fabry-Perot interferometers during ge-  
411 omagnetically quiet conditions: 1. Local time, latitudinal, seasonal, and solar cycle  
412 dependence, *Journal of Geophysical Research: Space Physics*, 111(12), 1–13, doi:  
413 10.1029/2006JA011948.
- 414 Fisher, D. J., J. J. Makela, J. W. Meriwether, R. A. Buriti, Z. Benkhaldoun, M. Kaab, and  
415 A. Lagheryeb (2015), Climatologies of nighttime thermospheric winds and tempera-  
416 tures from Fabry-Perot interferometer measurements: From solar minimum to solar  
417 maximum, *Journal of Geophysical Research A: Space Physics*, 120(8), 6679–6693, doi:  
418 10.1002/2015JA021170.
- 419 Harding, B. J., T. W. Gehrels, and J. J. Makela (2014), Nonlinear regression method for  
420 estimating neutral wind and temperature from Fabry-Perot interferometer data, *Applied*  
421 *Optics*, 53(4), 666, doi:10.1364/AO.53.000666.
- 422 Harding, B. J., J. Qin, and J. J. Makela (2017), Ground-Based Optical Measurements of  
423 Quiet Time Thermospheric Wind and Temperature: Atmospheric Scattering Correc-  
424 tions, *Journal of Geophysical Research: Space Physics*, 122(11), 11,624–11,632, doi:  
425 10.1002/2017JA024705.
- 426 Hernandez, G. (1974), Contamination of the OI(3P2-1D2) emission line by the (9-3) band  
427 of OH X2II in high-resolution measurements of the night sky, *Journal of Geophysical*  
428 *Research*, 79(7), 1119–1123, doi:10.1029/JA079i007p01119.
- 429 Liuzzo, L. R., A. J. Ridley, N. J. Perlongo, E. J. Mitchell, M. Conde, D. L. Hampton,  
430 W. A. Bristow, and M. J. Nicolls (2015), High-latitude ionospheric drivers and their  
431 effects on wind patterns in the thermosphere, *Journal of Geophysical Research: Space*  
432 *Physics*, 120(1), 715–735, doi:10.1002/2014JA020553.
- 433 Makela, J. J., D. J. Fisher, J. W. Meriwether, R. A. Buriti, and A. F. Medeiros (2013),  
434 Near-continual ground-based nighttime observations of thermospheric neutral winds  
435 and temperatures over equatorial Brazil from 2009 to 2012, *Journal of Atmospheric and*  
436 *Solar-Terrestrial Physics*, 103, 94–102, doi:10.1016/j.jastp.2012.11.019.
- 437 Makela, J. J., B. J. Harding, J. W. Meriwether, R. Mesquita, S. Sanders, A. J. Ridley,  
438 M. W. Castellez, M. Ciocca, G. D. Earle, N. A. Frissell, D. L. Hampton, A. J. Ger-  
439 rard, J. Noto, and C. R. Martinis (2014), Storm time response of the midlatitude ther-  
440 mosphere: Observations from a network of Fabry-Perot interferometers, *Journal of Geo-*  
441 *physical Research: Space Physics*, 119(8), 6758–6773, doi:10.1002/2014JA019832.
- 442 Mehta, P. M., A. C. Walker, E. K. Sutton, and H. C. Godinez (2017), New density esti-  
443 mates derived using accelerometers on board the CHAMP and GRACE satellites, *Space*  
444 *Weather*, 15(4), 558–576, doi:10.1002/2016SW001562.
- 445 Meriwether, J. W., J. J. Makela, Y. Huang, D. J. Fisher, R. A. Buriti, A. F. Medeiros, and  
446 H. Takahashi (2011), Climatology of the nighttime equatorial thermospheric winds  
447 and temperatures over Brazil near solar minimum, *Journal of Geophysical Research*,  
448 116(A4), 1–12, doi:10.1029/2011JA016477.
- 449 Meriwether, J. W., J. J. Makela, D. J. Fisher, R. Buriti, a.F. Medeiros, R. Akmaev,  
450 T. J. Fuller-Rowell, and F. Wu (2013), Comparisons of thermospheric wind and  
451 temperature measurements in equatorial Brazil to Whole Atmosphere Model Pre-  
452 dictions, *Journal of Atmospheric and Solar-Terrestrial Physics*, 103, 103–112, doi:

- 453 10.1016/j.jastp.2013.04.002.
- 454 Newell, P. T., K. Liou, Y. Zhang, T. Sotirelis, L. J. Paxton, and E. J. Mitchell (2014),  
455 OVATION Prime-2013: Extension of auroral precipitation model to higher disturbance  
456 levels, *Space Weather*, *12*(6), 368–379, doi:10.1002/2014SW001056.
- 457 Picone, J. M., A. E. Hedin, D. P. Drob, and A. C. Aikin (2002), NRLMSISE-00 empir-  
458 ical model of the atmosphere: Statistical comparisons and scientific issues, *Journal of*  
459 *Geophysical Research: Space Physics*, *107*(A12), 1–16, doi:10.1029/2002JA009430.
- 460 Ridley, A., Y. Deng, and G. Tóth (2006), The global ionosphere-thermosphere  
461 model, *Journal of Atmospheric and Solar-Terrestrial Physics*, *68*(8), 839–864, doi:  
462 10.1016/j.jastp.2006.01.008.
- 463 Ronskley, A. (2016), Optical remote sensing of mesoscale thermospheric dynamics above  
464 Svalbard and Kiruna, Ph.D. thesis, University of London.
- 465 Sutton, E. K., R. S. Nerem, and J. M. Forbes (2007), Density and Winds in the Thermo-  
466 sphere Deduced from Accelerometer Data, *Journal of Spacecraft and Rockets*, *44*(6),  
467 1210–1219, doi:10.2514/1.28641.
- 468 Taylor, K. E. (2001), Summarizing multiple aspects of model performance in a  
469 Single Diagram, *Journal of Geophysical Research*, *106*(D7), 7183–7192, doi:  
470 10.1029/2000JD900719.
- 471 Weimer, D. R. (2005), Improved ionospheric electrodynamic models and application  
472 to calculating Joule heating rates, *Journal of Geophysical Research: Space Physics*,  
473 *110*(A5), 1–21, doi:10.1029/2004JA010884.
- 474 Wu, Q., D. McEwen, W. Guo, R. Niciejewski, R. Roble, and Y.-I. Won (2008),  
475 Long-term thermospheric neutral wind observations over the northern polar cap,  
476 *Journal of Atmospheric and Solar-Terrestrial Physics*, *70*(16), 2014–2030, doi:  
477 10.1016/j.jastp.2008.09.004.
- 478 Wu, Q., B. A. Emery, S. G. Shepherd, J. M. Ruohoniemi, N. A. Frissell, and J. Seme-  
479 ter (2015), High-latitude thermospheric wind observations and simulations with  
480 SuperDARN data driven NCAR TIEGCM during the December 2006 magnetic  
481 storm, *Journal of Geophysical Research: Space Physics*, *120*(7), 6021–6028, doi:  
482 10.1002/2015JA021026.

Figure 1.

Author Manuscript

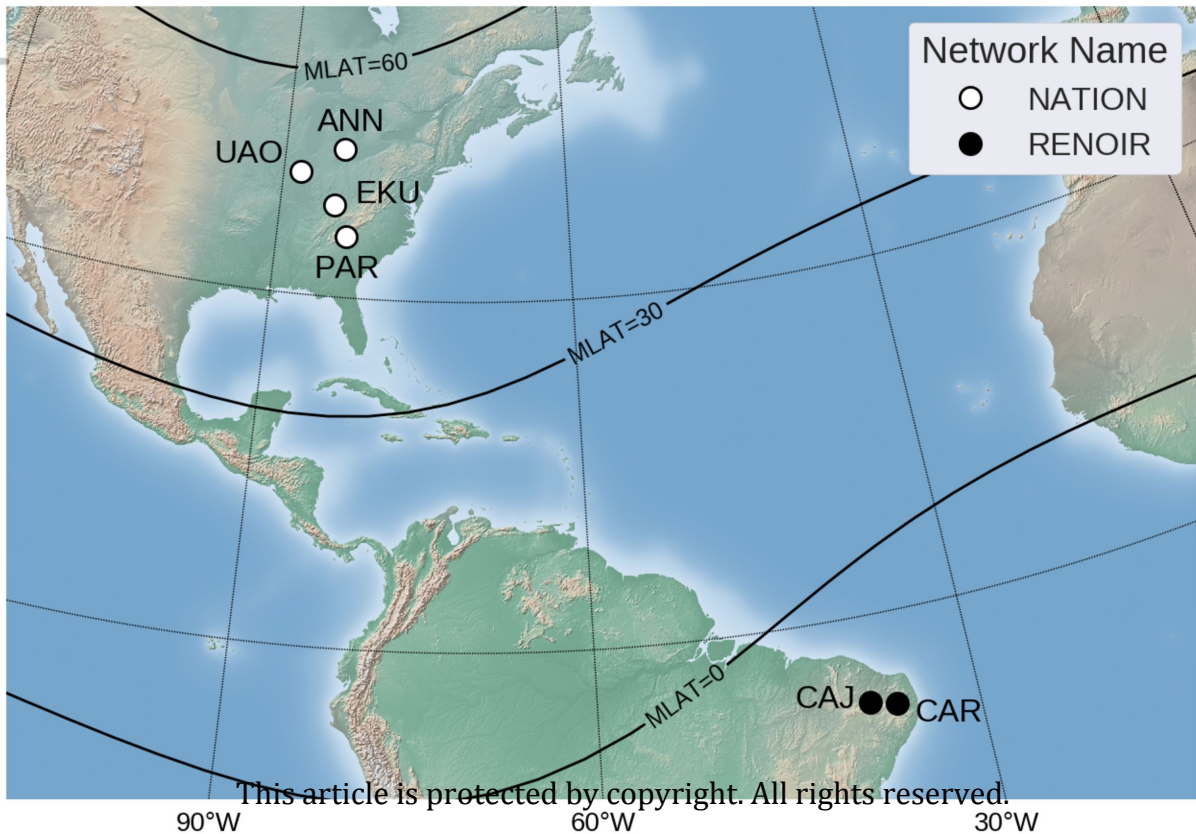
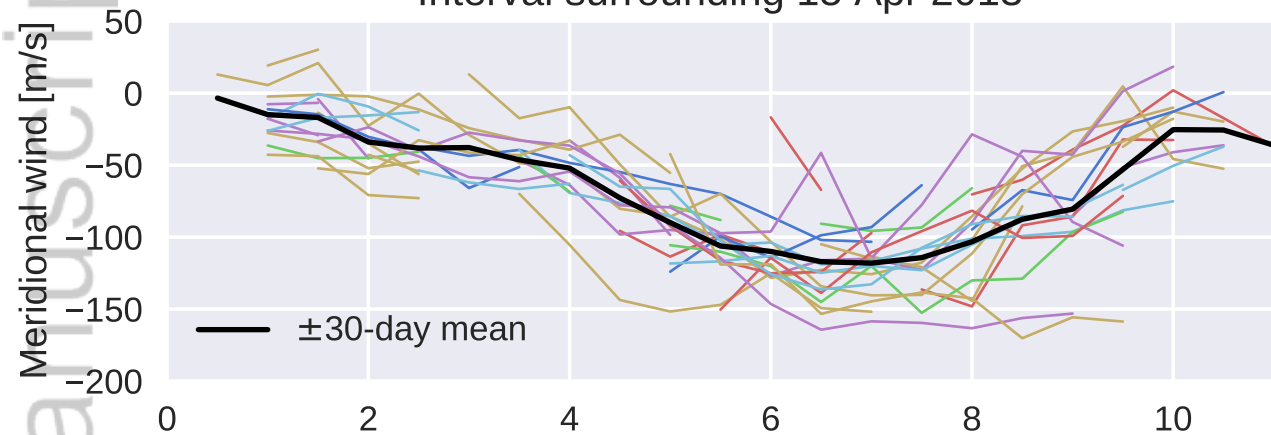




Figure 2.

Author Manuscript

Data (FPI at PAR)  
Interval surrounding 15 Apr 2013



Model (GITM at PAR)

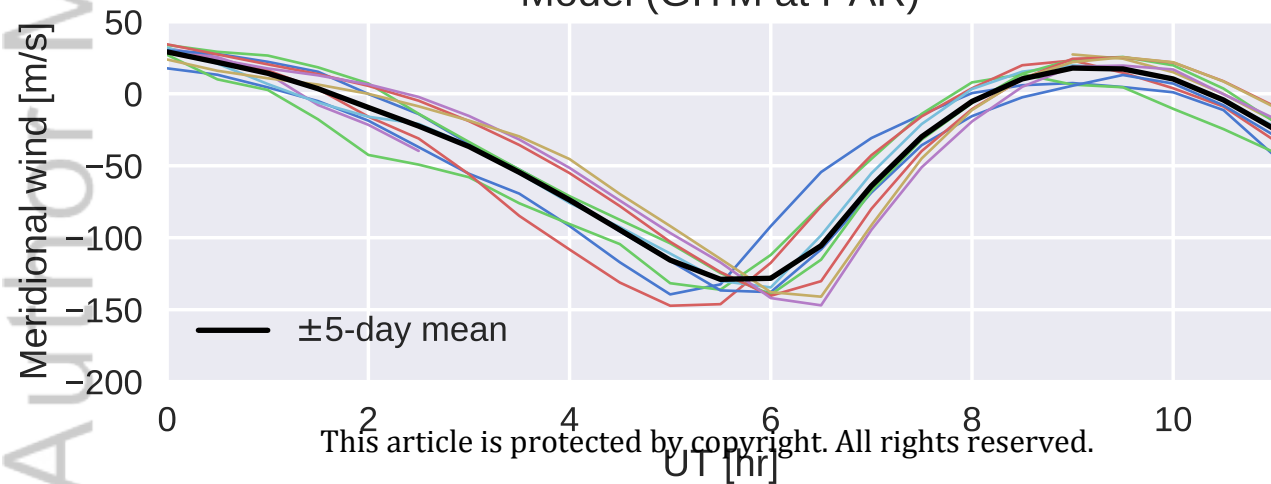


Figure 3.

Author Manuscript

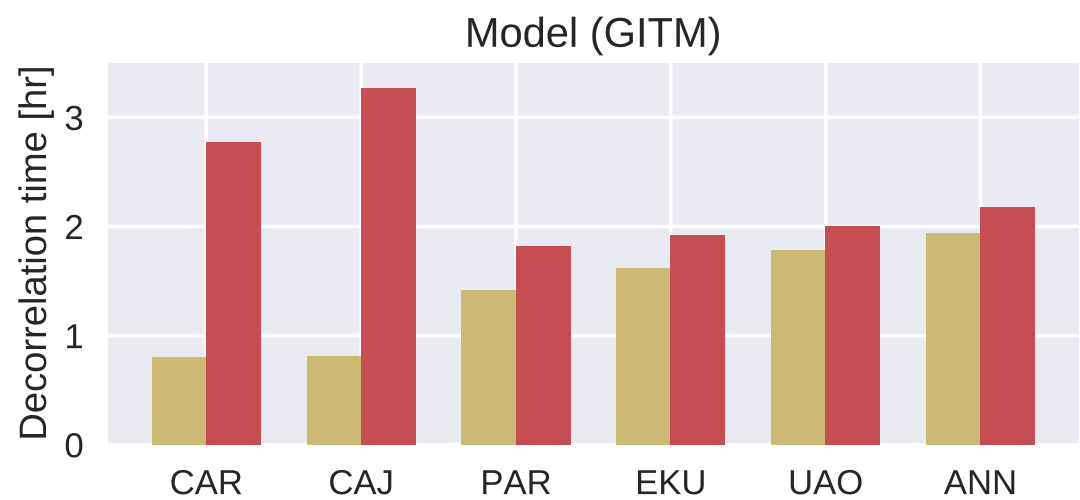
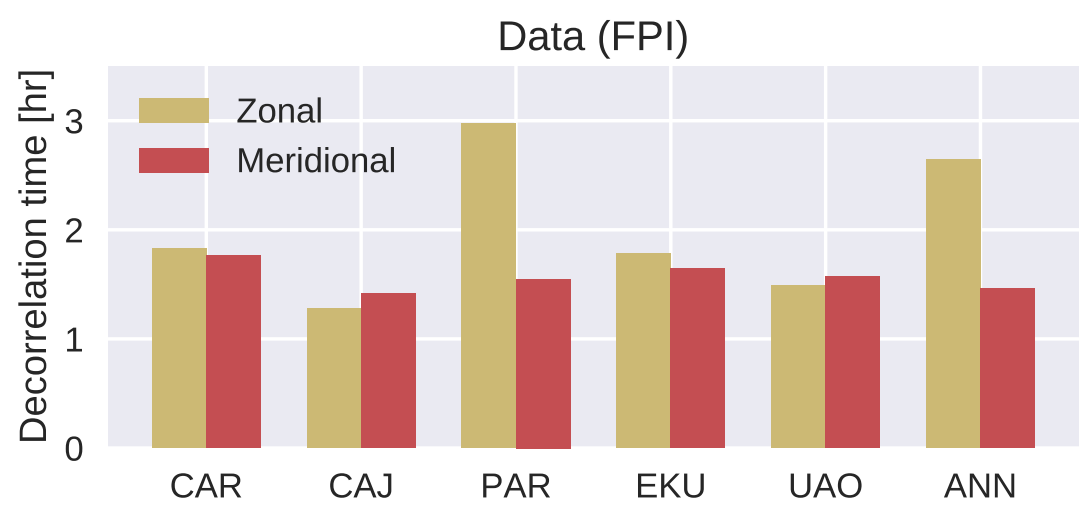
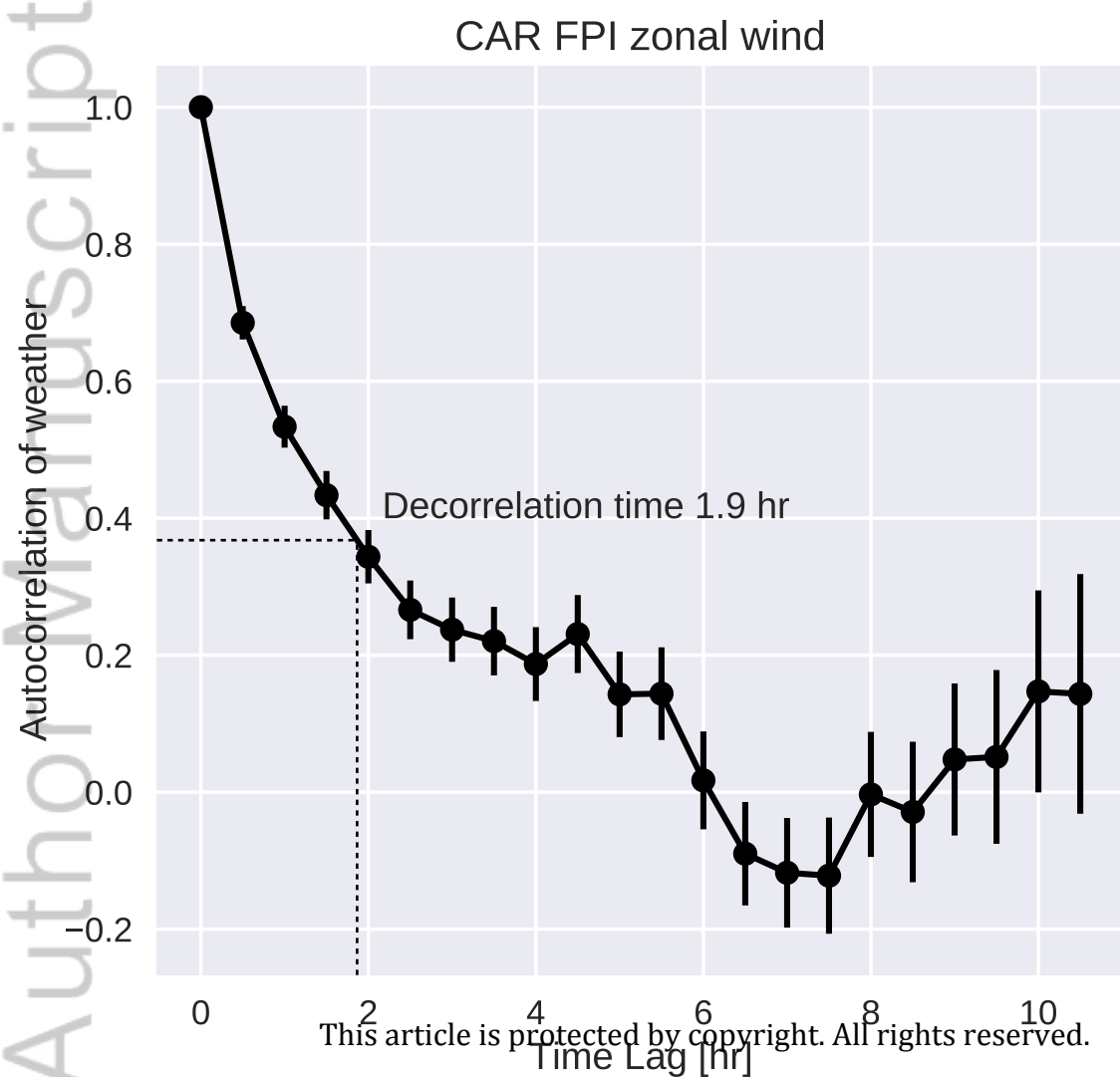


Figure 4.

Author Manuscript

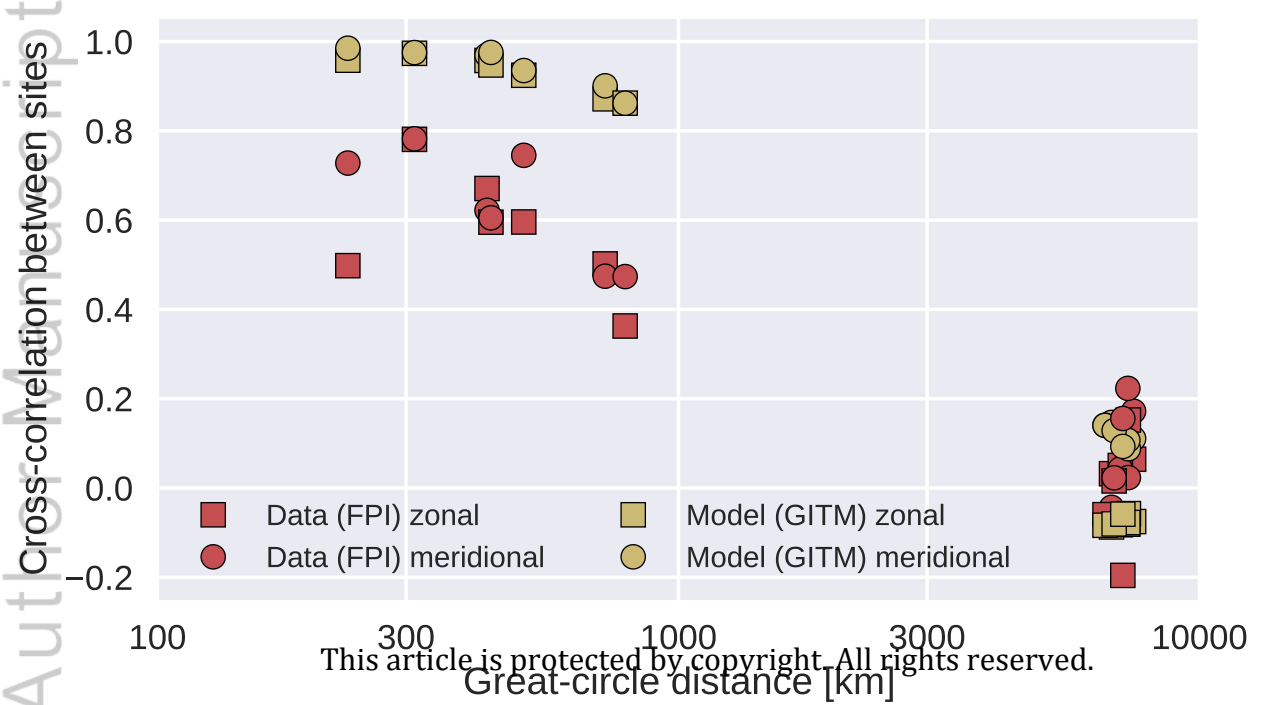
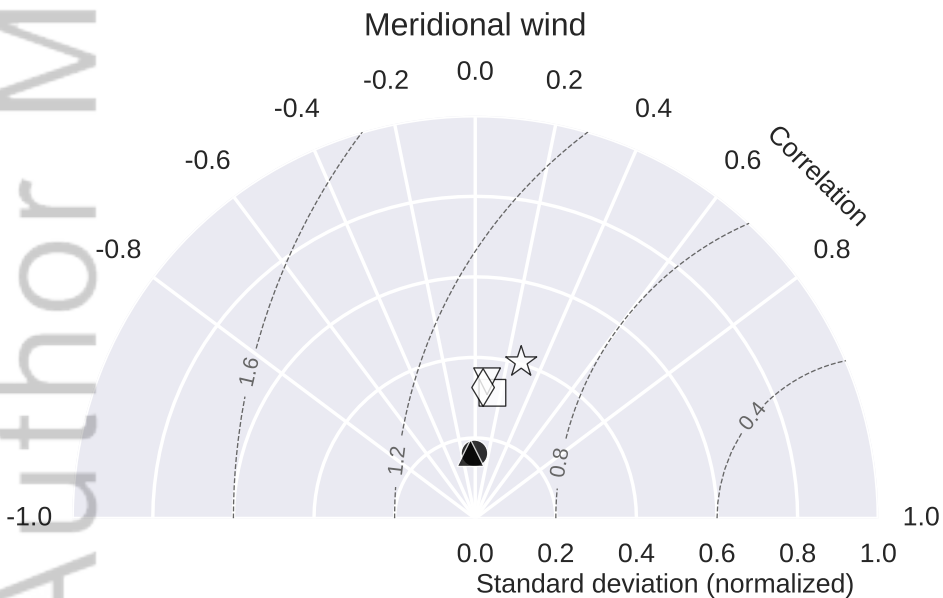
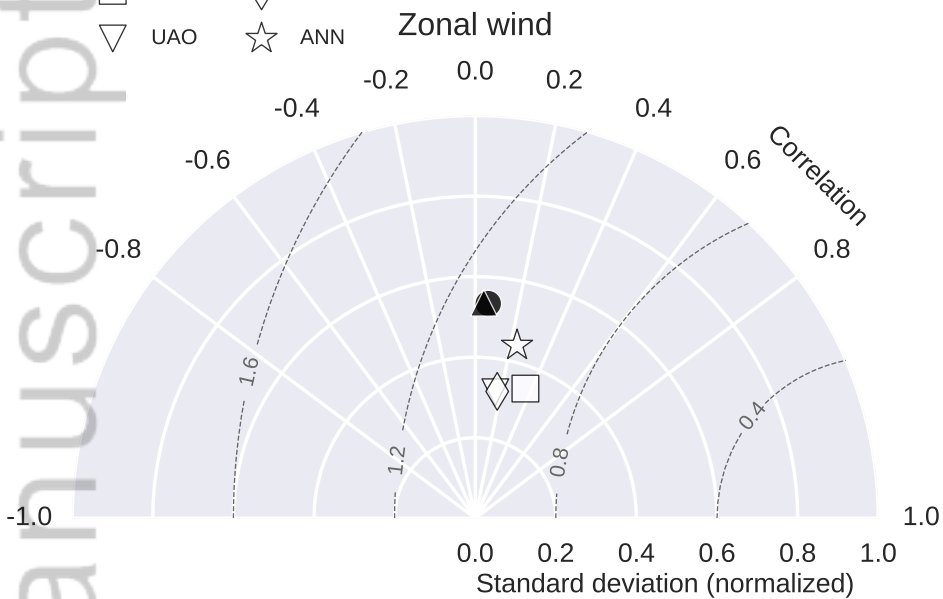


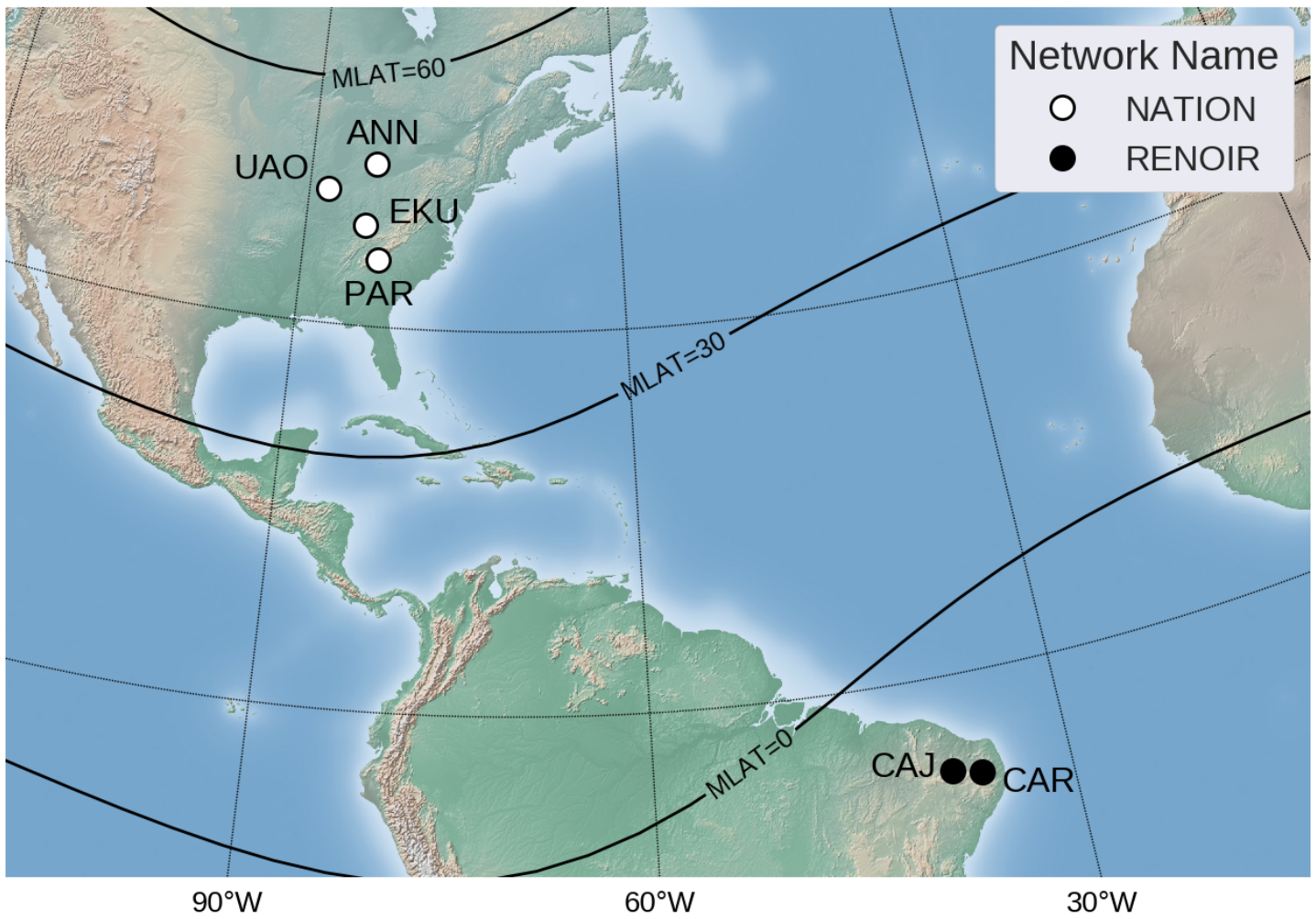
Figure 5.

Author Manuscript

- CAR
- ▲ CAJ
- PAR
- ◇ EKU
- ▽ UAO
- ☆ ANN

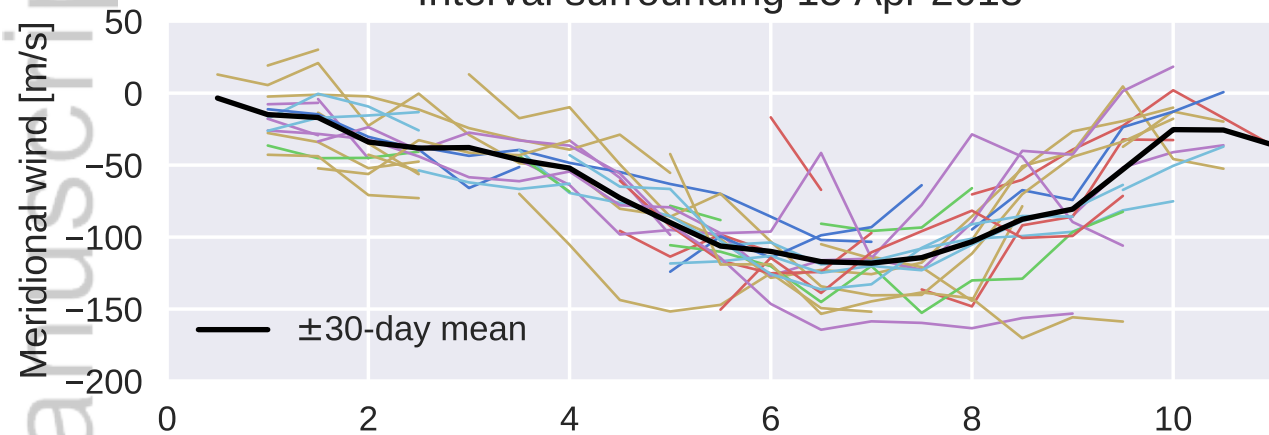




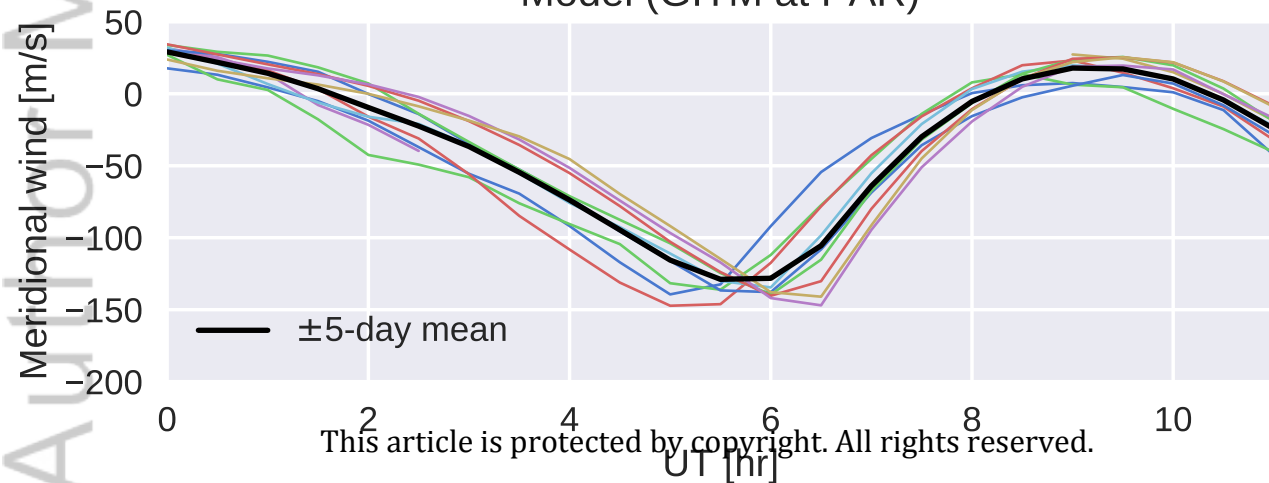


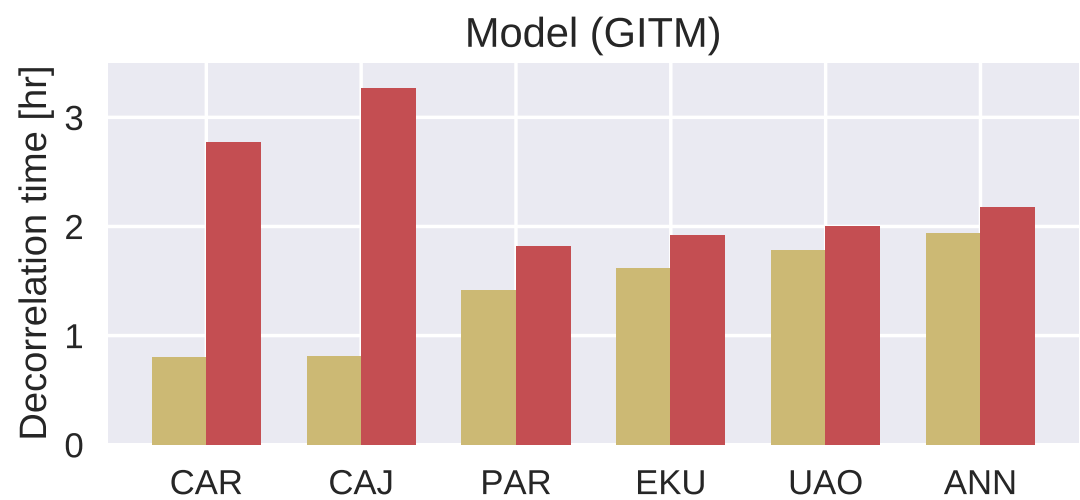
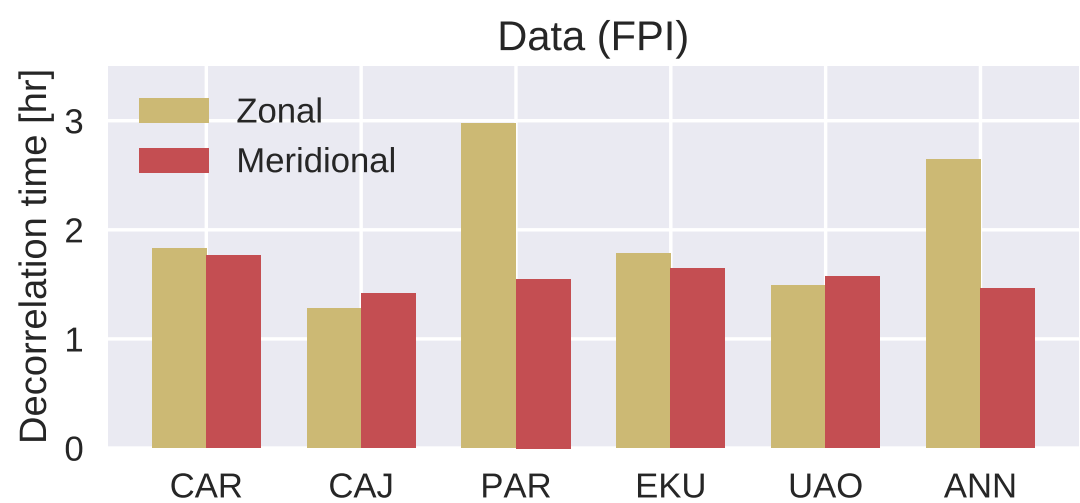
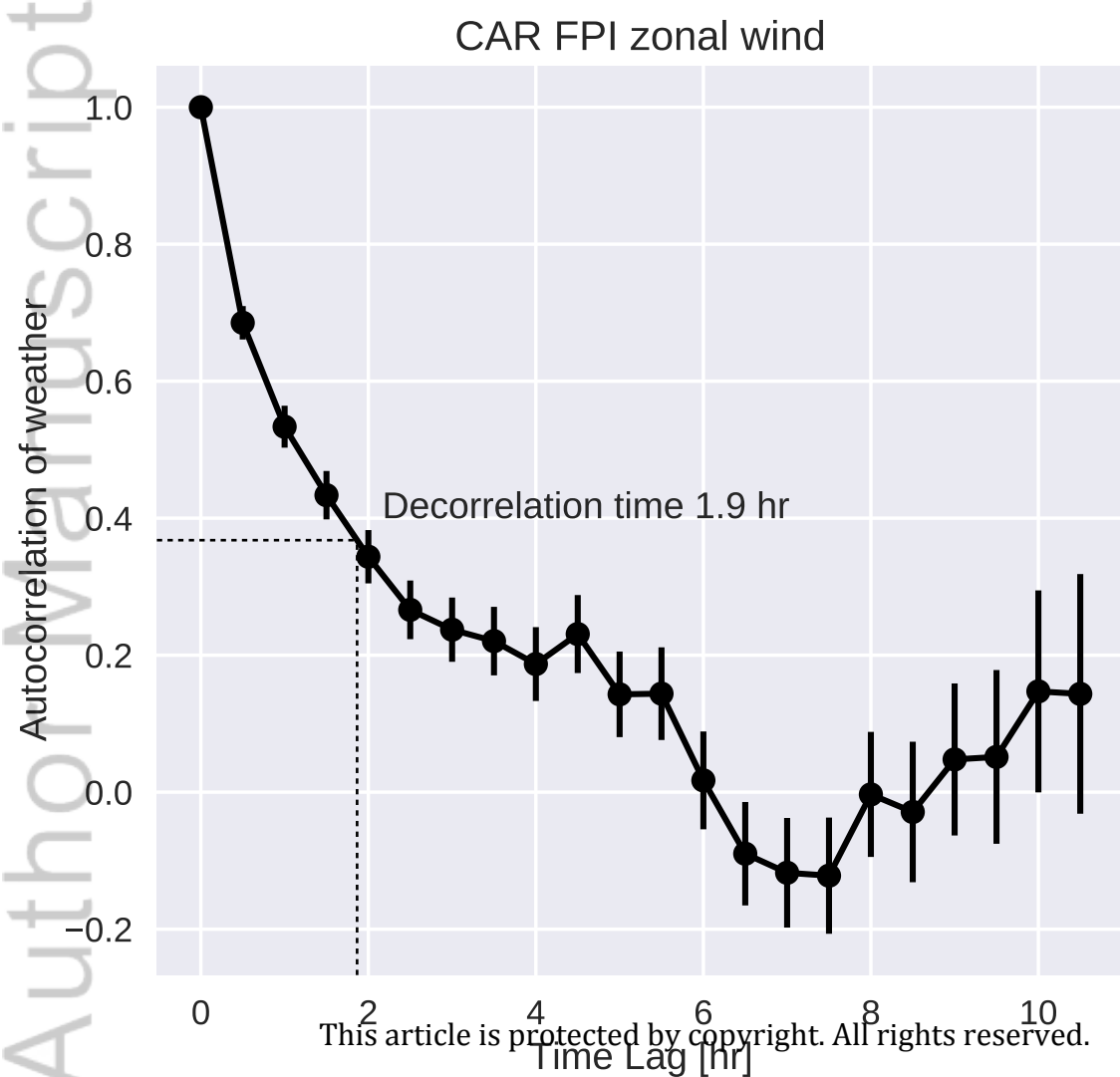
2018JA026032-f01-z-.png

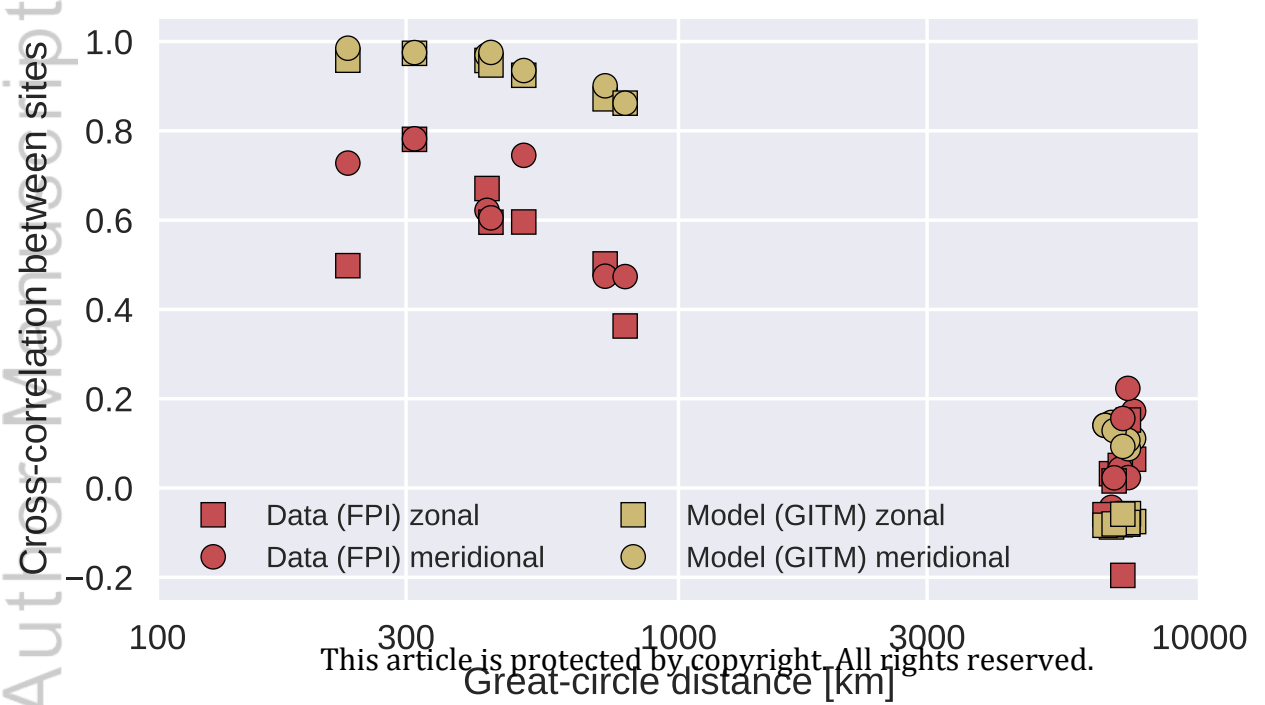
Data (FPI at PAR)  
Interval surrounding 15 Apr 2013



Model (GITM at PAR)







- CAR
- ▲ CAJ
- PAR
- ◇ EKU
- ▽ UAO
- ☆ ANN

